ACS OMEGA

http://pubs.acs.org/journal/acsodf

Article

Tin Oxide/Vertically Aligned Graphene Hybrid Electrodes Prepared by Sonication-Assisted Sequential Chemical Bath Deposition for High-Performance Supercapacitors

Na Eun Lee, Seung Uk Cheon, Jaewoo Lee, and Sung Oh Cho*

Cite This: *ACS Omega* 2023, 8, 6621−6631

Read Online

ACCESS | Metrics & More | Article Recommendations | Supporting Information

ABSTRACT: Hybrid electrodes comprising metal oxides and vertically aligned graphene (VAG) are promising for high-performance supercapacitor applications because they enhance the synergistic effect owing to the large contact area between the two constituent materials. However, it is difficult to form metal oxides (MOs) up to the inner surface of a VAG electrode with a narrow inlet using conventional synthesis methods. Herein, we report a facile approach to fabricate SnO_2 nanoparticle-decorated VAG electrodes (SnO_2@VAG) with excellent areal capacitance and cyclic stability using sonication-assisted sequential chemical bath deposition (S-SCBD). The sonication treatment during the MO decoration process induced a cavitation effect at the narrow inlet of the VAG electrode, allowing the precursor solution to reach the inside of the VAG surface. Furthermore, the sonication treatment promoted MO nucleation on the entire VAG surface. Thus, the SnO_2 nanoparticles uniformly covered the entire electrode surface after the S-SCBD process. SnO_2@VAG exhibited an outstanding areal capacitance (4.40 F cm^{-2}) up to 58% higher than that of VAG electrodes. The symmetric supercapacitor with SnO_2@VAG electrodes showed an excellent areal capacitance (2.13 F cm^{-2}) and a cyclic stability of 90% after 2000 cycles. These results suggest a new avenue for sonication-assisted fabrication of hybrid electrodes in the field of energy storage.

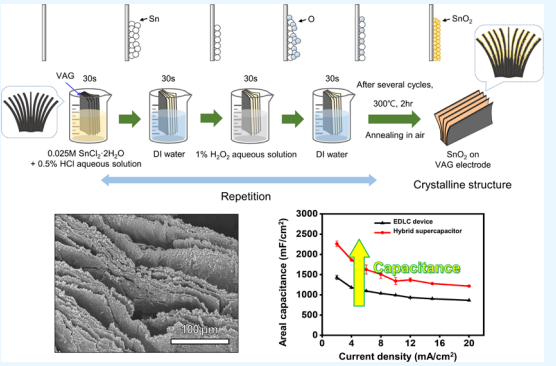

1. INTRODUCTION

Supercapacitors have received considerable attention in the field of energy storage because of their high power densities, fast charging/discharging rates, and long life cycles.[1,2] Supercapacitor electrodes can be classified into three types depending on their energy-storage mechanism: electric double-layer capacitors (EDLCs), pseudocapacitors, and hybrid electrodes.[3,4] EDLCs, which are based on the physical accumulation of charged species on the electrode surface, have a high power density; however, their energy density is low.[3,5] Carbon-based materials are commonly used for fabricating EDLC electrodes because of their large specific surface area (SSA) and superior electrical conductivity.[1,6] Among them, graphene has attracted interest owing to its excellent electrical conductivity with a large SSA.[7] Pseudocapacitors, which store energy through surface redox or Faradaic reactions, exhibit higher energy densities than EDLCs.[3] Despite this advantage, their low power density and poor cyclic stability degrade their representative features, thus limiting widespread usage.[8] They mainly use transition metals (oxides) and conductive polymers for electrode manufacturing.[9] Hybrid electrodes, which combine EDLCs and pseudocapacitors, have an improved energy density as well as excellent power density and overcome the drawbacks of each electrode type owing to the synergistic effect of the two constituent materials, such as the cyclic stability of pseudocapacitors.[10] According to recent reports, the fabrication of hybrid electrodes with metal oxides (MOs) as pseudocapacitive materials and graphene as the EDLC material is effective for drastically improving the energy density.[11] Hybrid electrodes using MOs have the advantage of increasing the energy density without requiring treatment to reinforce the interfacial interaction between adjacent materials,[12,13] unlike the case where a conducting polymer is used, which is another representative pseudocapacitive material.[14] Many studies have reported the fabrication of MO/graphene hybrid electrodes using hydrothermal methods having a simple procedure,[15] microwave-assisted synthesis providing rapid synthesis,[16] electrochemical deposition,[17] laser processing,[18] and chemical bath deposition (CBD).[19] The electrochemical deposition and laser processing can control the surface structure, size, and shape of the electrode elaborately by controlling the electrochemical conditions.[20] CBD, with a simple process, has the advantage of being able to be performed at a low temper-

Received: November 2, 2022
Accepted: January 26, 2023
Published: February 8, 2023

https://doi.org/10.1021/acsomega.2c07075
ACS Omega 2023, 8, 6621−6631

ature.[21] These synthesis methods are variously used in the synthesis of hybrid electrodes according to the manufacturing requirements.

In our previous study, we demonstrated the outstanding electrochemical performance of an EDLC with vertically aligned graphene (VAG) as an electrode. The VAG electrode, which comprises graphene sheets aligned perpendicular to the electrode surface, has a higher energy density and a larger SSA than other graphene electrodes owing to its unique 3D structure.[22] This 3D structure helps prevent restacking of the adjacent graphene sheets and promotes smooth ion transfer, resulting in a drastic increase in the SSA and energy density.[23] Therefore, in this study, a hybrid electrode was fabricated to attach MO particles onto the VAG surface to maximize the energy density growth. The most important factor in fabricating a hybrid capacitor with a VAG electrode is uniformly covering the entire VAG surface with MO particles. The uniform coverage of MO on the VAG electrode with a narrow inlet enhances the synergistic effect between MO and graphene over a wide area, thereby dramatically increasing the energy density.[24] However, there are limitations in uniformly covering MOs on the entire electrode surface with a narrow inlet structure, even when using conventional solution-based methods.[25] In the conventional method, it is difficult to produce MO particles that can penetrate the narrow inlet of the electrode using the precursor solution because of its high surface tension.[25] Therefore, the MO particles form an agglomerate only at the inlet of the electrode, resulting in a loss of structural advantage of VAG and limiting the increase in its energy density. Thus, a new method is required to fabricate a hybrid electrode capable of uniformly forming MO particles up to the inner surface of the electrode having a narrow inlet.

In this study, we propose a simple approach for fabricating a hybrid electrode by decorating SnO_2 nanoparticles on a VAG surface using sonication-assisted sequential CBD (S-SCBD). The S-SCBD is a method for sequentially immersing an electrode in cationic and anionic precursor solutions using ultrasonication treatment.[25,26] The ultrasonication treatment performed during the synthesis causes a cavitation effect at the narrow inlet of the VAG electrode.[27] This cavitation effect allows the precursor solution to penetrate the interior of the VAG and increase the wettability of the surface, resulting in the formation of MO particles up to the inside surface.[27,28] The intense microconvention produced by sonication facilitates the formation of active nucleation sites for MO nanoparticles, promoting MO formation at numerous sites.[29] Furthermore, the sonication treatment suppresses the growth of MO grains, resulting in uniform nucleation of the MO nanoparticles and limiting the particle growth.[30] Thus, numerous MO nanoparticles may be uniformly formed on the entire surface of the VAG electrode without being aggregated in a specific region. As described above, the S-SCBD method has the potential to effectively form MO nanoparticles on the electrode surface, regardless of the surface morphology and enable mass production via a simple process.

In this study, tin oxide (SnO_2) nanoparticles were used as MO particles to produce hybrid electrodes. Several MOs, including RuO_2,[31] MnO_2,[32] NiO,[33] Co_3O_4,[34] NiSe,[35] MoS_2,[36] and SnO_2,[13,37] have been used to manufacture supercapacitor electrodes. Among them, SnO_2 has attracted wide attention owing to its low cost, high power density, environmentally friendly characteristics, and superior energy density (~782 mA h g^{-1}).[13,38,39] Based on these properties, SnO_2 is mainly used for the fabrication of energy-storage devices such as Li-ion batteries and supercapacitors.[40,41] However, SnO_2 has some critical drawbacks, such as low electrical conductivity and poor cyclic stability.[40,42] Fabrication of the hybrid electrode combining SnO_2 and a carbon-based material not only solves these problems but also improves the electrochemical performance.[42] Therefore, recent studies have reported the preparation of hybrid electrodes for a high-performance supercapacitor by utilizing SnO_2 and carbon-based materials such as graphene.[39,43]

Hybrid electrodes with VAG were fabricated using the S-SCBD method, and a symmetric supercapacitor with SnO_2 nanoparticle-decorated VAG electrodes (SnO_2@VAG) was prepared. The areal capacitance of the VAG electrode-based hybrid capacitor increased following the S-SCBD application. The symmetric supercapacitor showed superior cyclic stability and energy density for up to 2000 cycles.

2. EXPERIMENTAL SECTION

2.1. Materials. Graphite foil (GF, thickness: 3 mm, 99.9%), purchased from Shinsung Carbon (Anyang, Korea), was used to manufacture the VAG electrode. All chemicals (ethanol, NH_4F, KCl, H_2O_2, and $SnCl_2{\cdot}2H_2O$) used as electrolytes to synthesize the VAG electrode and precursors in the S-SCBD method were purchased from Sigma-Aldrich.

2.2. Fabrication of VAG Electrodes. The VAG electrode was fabricated by electrochemical anodization using GF, as reported previously.[22] GF electrodes were produced, in which two pieces of rectangular GF [3 mm × 20 mm ($w \times h$)] were adhered using carbon tape, and the other sides that were not anodized were insulated using Kapton tape. VAG electrodes were synthesized using a two-electrode anodization system using the GF electrode and Pt foil [1 cm × 1.2 cm × 0.02 cm ($w \times h \times t$)] as the anode and the cathode, respectively. A constant dc voltage of +10 V was applied to the two electrodes immersed in a 0.1 M NH_4F aqueous solution at 25 °C. The distance between the two electrodes was 3 cm, and the electrochemical anodizing duration was 60 min. After anodization, the VAG electrodes were washed with deionized water for a few minutes and then dried in a vacuum oven at 50 °C for 1 h.

2.3. Fabrication of SnO_2@VAG Using the S-SCBD Method. The VAG surface was decorated with SnO_2 nanoparticles using the S-SCBD approach. $SnCl_2{\cdot}2H_2O$ and H_2O_2 aqueous solutions were used as cationic and anionic precursor solutions for forming SnO_2 on the VAG electrode, respectively. We added 0.5641 g of $SnCl_2{\cdot}2H_2O$ particles and 1% HCl solution to deionized water. This solution was then stirred for 30 min at room temperature to dissolve the particles to prepare 100 mL of 0.025 M $SnCl_2{\cdot}2H_2O$ aqueous solution. First, the VAG electrode was immersed in 0.025 M $SnCl_2{\cdot}2H_2O$ solution for 30 s so that the precursor could be attached to the VAG electrode, which was then rinsed in deionized water for 30 s to remove the excess reagent. Thereafter, the VAG electrode was immersed in 100 mL of 1% H_2O_2 solution for 30 s, and the electrode was rinsed in deionized water for 30 s to remove the excess ions. Ultrasonication treatment was performed during all of the immersing and rinsing processes with an Ultrasonic Cleaner Set (WUC-A01H, DAIHAN Scientific Co., Ltd., South Korea). The ultrasonic power and hertz were 158 W and 60 Hz, respectively. The entire process of dipping the VAG electrode in four beakers in order was done in one cycle, and the sample subjected to X cycles was

https://doi.org/10.1021/acsomega.2c07075
ACS Omega 2023, 8, 6621−6631

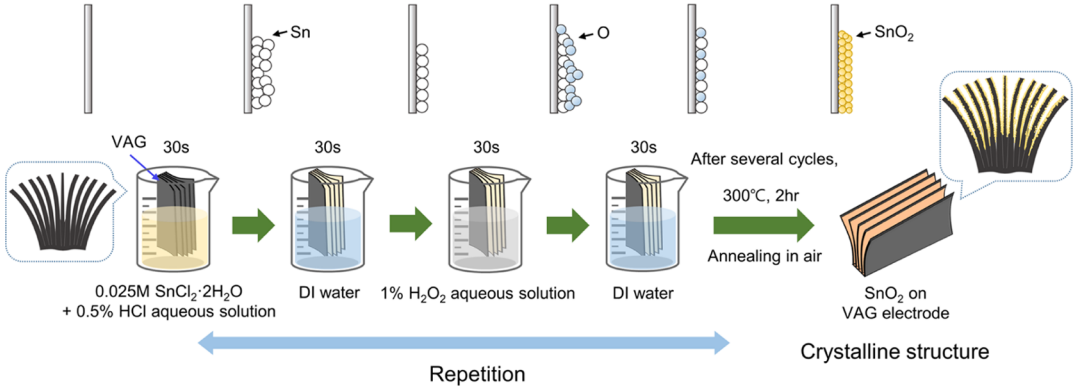

Figure 1. Schematic illustration of preparation of the VAG electrodes decorated with SnO_2 nanoparticles using the S-SCBD process.

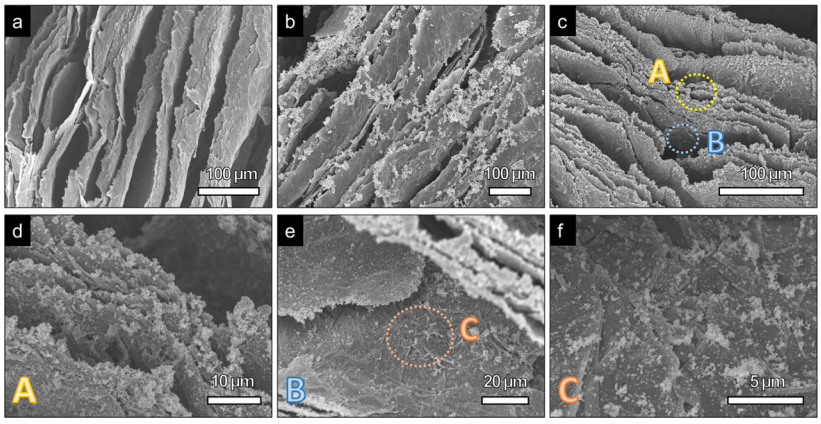

Figure 2. FE-SEM images of the top-view morphology of (a) VAG electrode, (b) SnO_2@VAG-15 fabricated by the sequential CBD process without the sonication process, (c) SnO_2@VAG-15 produced by the S-SCBD process, (d) edges of SnO_2@VAG-15 [part A in (c)], (e) inside the surface of SnO_2@VAG-15 [part B in (c)], and (f) magnified inside the surface of SnO_2@VAG-15 [part C in (e)].

referred to as SnO_2@VAG-X. The VAG electrodes after the S-SCBD method were dried in a vacuum oven at 50 °C for 2 h. After drying, they were annealed in an oven at 300 °C in air for 2 h.

2.4. Assembly of the Symmetric Supercapacitor Device. The symmetric supercapacitor device was fabricated as a symmetric device using two pieces of SnO_2@VAG-15. SnO_2@VAG-15 soaked in a 3 M KCl aqueous solution for 10 min and a cellulose acetate membrane (MCA) filter were used as the electrode and the separator, respectively. The anodized surfaces of the two pieces of SnO_2@VAG-15 were attached such that they faced each other, and the MCA separator was inserted between these electrodes. The devices were wrapped with Parafilm to prevent electrolyte leakage. The entire volume of the device was approximately 0.50 cm^3.

2.5. Characterization of the VAG and SnO_2@VAG Electrodes. The surface morphologies of the VAG electrode and SnO_2@VAG were measured using field-emission scanning electron microscopy (FE-SEM; SU8230, Hitachi, Tokyo, Japan) at an accelerating voltage of 15 kV. The atomic ratio of SnO_2 on the VAG surface was assessed using energy-dispersive X-ray spectroscopy (EDS) attached to scanning electron microscopy (SEM). The crystallinity and interlayer spacing of the electrodes were obtained using high-resolution transmission electron microscopy (HRTEM, Tecnai G2 F30 S-Twin, FEI, USA) at an accelerating voltage of 200 kV. Raman spectroscopy of the electrodes was performed to determine their crystallinity using a micro-Raman spectrometer (Horiba Jobin Yvon, France) equipped with a 514 nm laser source of spot size 2 μm. Chemical analyses of the VAG electrode and SnO_2@VAG were performed using X-ray photoelectron spectroscopy (XPS) and Fourier transform infrared (FT-IR) spectroscopy. The XPS results of the electrodes were recorded to determine the bonding state and atomic ratio of the electrode surfaces. A micro-focused monochromatic X-ray source operated at 3000 W (Al Kα, Thermo VG Scientific, USA) was used for the XPS measurements. The chemical bonds in the VAG and SnO_2@VAG electrodes were evaluated by FT-IR spectroscopy using a Nicolet iS50 spectrometer (Thermo Fisher Scientific, USA). The wettability test of the VAG electrode was performed by measuring the contact angle of the water droplets on the electrode surface using a CCD camera (software; Rame-Hart Instruments Co., USA). The crystallinity of the VAG electrodes before and after S-SCBD was determined using thin-film X-ray diffractometry (XRD, Ultima IV, RIGAKU, Tokyo, Japan).

2.6. Electrochemical Properties of the Electrode and the Supercapacitor Device. Electrochemical performance tests were performed on the VAG electrode and SnO_2@VAG using a three-electrode system with an SP-200 instrument (BioLogic, France). In these measurements, a VAG and SnO_2@VAG electrode (1 cm^2) served as the working electrode, and Pt foil (1 cm × 1 cm) and a saturated calomel electrode (SCE) were used as the counter and reference electrodes, respectively. The electrolyte was a 3 M KCl aqueous solution (Figures 2–6).

https://doi.org/10.1021/acsomega.2c07075
ACS Omega 2023, 8, 6621−6631

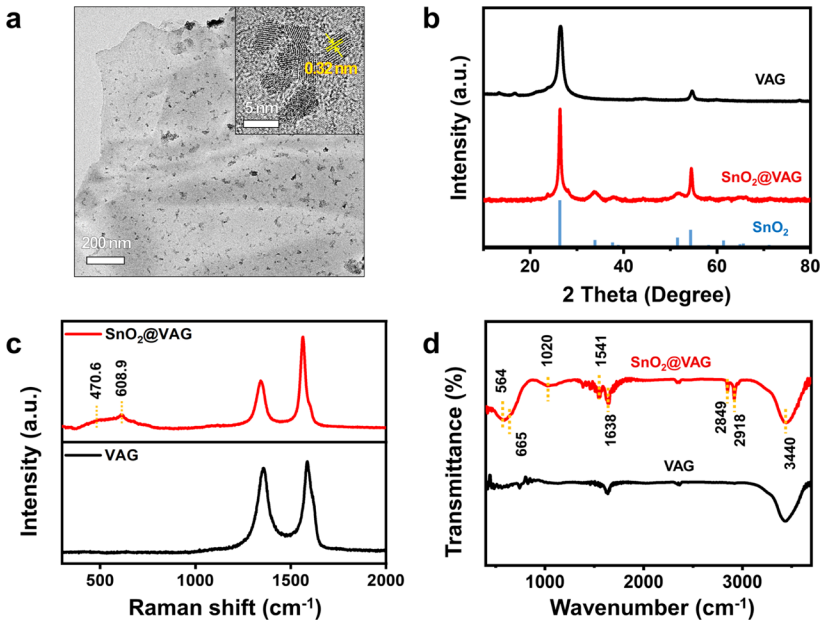

Figure 3. (a) TEM image of SnO_2@VAG-15 (inset: HRTEM image of SnO_2@VAG-15 showing the interlayer spacing). (b) XRD patterns of VAG, SnO_2@VAG-15, and SnO_2 according to the JCPDS file no. 41-1445. (c) Raman spectra and (d) FT-IR results of the VAG electrodes and SnO_2@VAG-15.

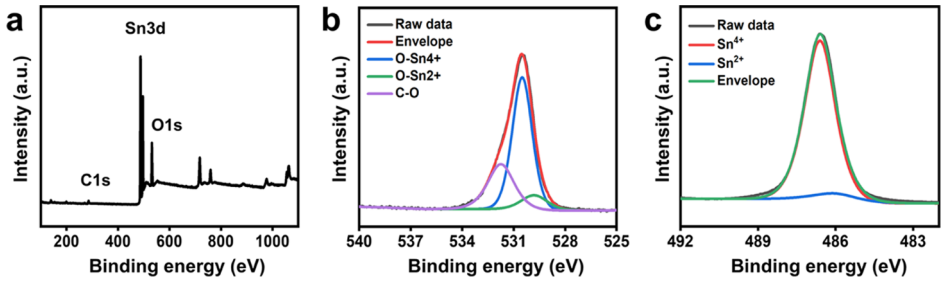

Figure 4. (a) XPS survey spectrum of SnO_2@VAG-15. (b) High-resolution O 1s and (c) Sn 3d spectra of SnO_2@VAG-15 with deconvoluted components.

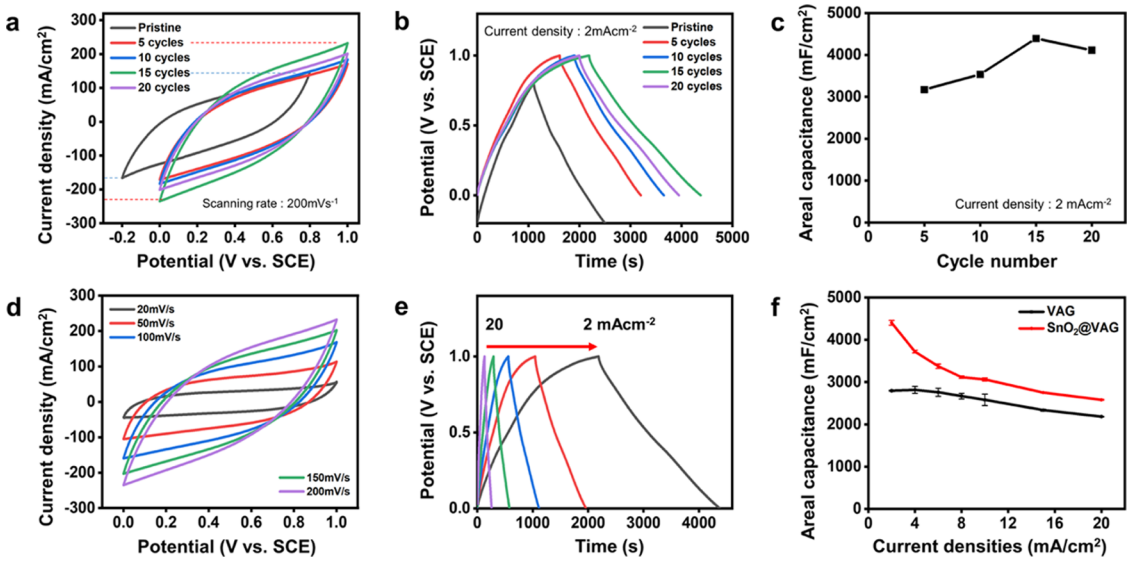

Figure 5. (a) CV curves and (b) GCD curves of VAG electrodes and SnO_2@VAG with different decorating times obtained at a scanning rate of 200 mV s^{-1} and a current density of 2 mA cm^{-2}. (c) Variation of the areal capacitance of SnO_2@VAG with decorating time obtained at a current density of 2 mA cm^{-2}. (d) CV curves and (e) GCD curves of SnO_2@VAG-15 at different scanning rates from 20 to 200 mV s^{-1} and current densities from 2 to 20 mA cm^{-2}. (f) Variation of the areal capacitance of the VAG electrode and SnO_2@VAG-15 with current densities.

https://doi.org/10.1021/acsomega.2c07075
ACS Omega 2023, 8, 6621−6631

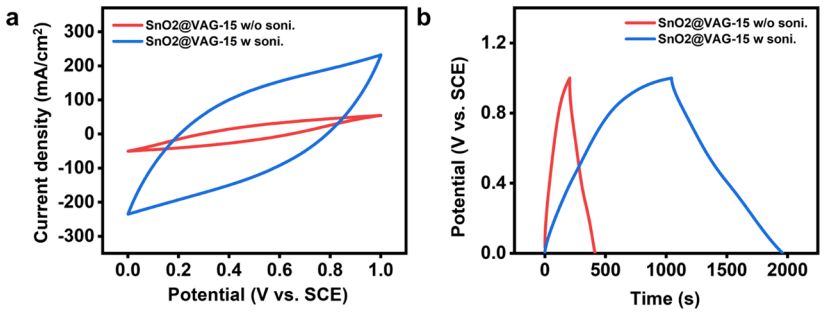

Figure 6. (a) CV curves and (b) GCD curves of SnO_2@VAG-15 with the sonication process and SnO_2@VAG-15 without the sonication process acquired at a scanning rate of 200 mV s^{-1} and a current density of 4 mA cm^{-2}.

The electrochemical properties of the VAG electrode and SnO_2@VAG were evaluated by cyclic voltammetry (CV) over a scanning rate range of 20−200 mV s^{-1} and galvanostatic charging/discharging (GCD) over potential ranges of −0.2 to 0.8 V (VAG) and 0−1 V (SnO_2@VAG). The electrochemical performance of the devices was determined using a two-electrode system with a 3 M KCl aqueous solution as the electrolyte, and the potential range was 0−1.2 V. The cyclic stability of the device was evaluated through cycle tests using GCD measurements at a current density of 20 mA cm^{-2}. Electrochemical impedance spectroscopy (EIS) of the device was performed at frequencies ranging from 10 mHz to 100 kHz at a potential amplitude of 5 mV.

3. RESULTS AND DISCUSSION

3.1. Characterizations of SnO_2@VAG. Figure 1 illustrates the preparation of SnO_2@VAG using the S-SCBD process. The VAG electrode was sequentially immersed in cationic and anionic precursor solutions for 30 s. When VAG was immersed in a cationic aqueous solution, the Sn^{4+} ions in the cationic solution adhered to the VAG surface, following eq 1.[44] The excess Sn^{4+} ions attached to the VAG surface were removed by rinsing with deionized water. The VAG electrode immersed in H_2O_2 aqueous solution underwent a reaction as described in eq 2, resulting in amorphous SnO_2 nanoparticles on the surface.[44] Similar to the previous step, the excess ions on the VAG surface were removed by rinsing with deionized water. Repeated cycles of the S-SCBD process were applied to the VAG electrode, and a large number of amorphous SnO_2 nanoparticles uniformly attached to the VAG surface. The SnO_2 nanoparticles on the VAG surface, which were annealed in air, became highly crystalline. In this process, the sonication process allowed the Sn precursor to reach the inner surface of the VAG. Thus, SnO_2 nanoparticle formation could occur on the entire VAG surface.

$$Sn^{4+} + 4H_2O \rightarrow Sn(OH)_4 + 4H^+ \quad (1)$$

$$Sn(OH)_4 + H_2O_2 \rightarrow SnO_2 + 3H_2O + \frac{1}{2}O_2 \quad (2)$$

Figure 2 shows the top-view morphologies of the VAG electrode, SnO_2@VAG-15 fabricated by sequential CBD without sonication, and SnO_2@VAG-15 produced by the S-SCBD process. The VAG electrode has a structure in which each graphite layer is separated from the adjacent graphite layer and vertically aligned from the bottom (Figure 2a). The average thickness of the VAG electrode is 4.6 mm. After the sequential CBD process, a large number of SnO_2 nanoparticles appeared on the VAG surface (Figure 2b,c). However, in the VAG electrode that had undergone SnO_2 decoration process without an ultrasonic environment, SnO_2 nanoparticles formed densely only at the edges of the graphite layers and were aggregated to block the expanded space between the graphite layers. Each separated graphite layer stuck without maintaining a distance due to the cohesion between SnO_2 nanoparticles formed at the edge. The VAG electrode, in which sonication was continuously performed during the SnO_2 decoration process, exhibits a different morphology. Nano-sized SnO_2 particles were uniformly attached along the edge of SnO_2@VAG-15 as well as on the entire surface inside the inlet and did not block the expanded space between the graphite layers (Figure 2d−f). The average amount of SnO_2 particles formed on the VAG surface was measured to be 28.64 mg/cm^2 and the average weight of SnO_2@VAG per area was 391.32 mg/cm^2. In particular, the SnO_2 nanoparticles shown in Figure 2c were smaller and highly homogeneous compared with those shown in Figure 2b. The sonication treatment may have caused a cavitation effect at the narrow inlet of the VAG, increasing the wettability of the VAG surface and reducing the surface tension of the precursor solution.[27,28] Therefore, the precursor solution reached the surface inside the VAG, and SnO_2 nanoparticles were formed on its surface. In addition, the sonication treatment inhibited the growth of SnO_2 grains, and thus, smaller and homogeneous nanoparticles were attached onto the entire surface without nanoparticle agglomeration along the VAG edges.[25,30] Therefore, the sonication process during SnO_2 decoration maximized the synergistic effect between graphene and SnO_2 by expanding the interfacial interaction area without reducing the entire surface area of the electrode.

Figure 2c−f and Figures S1−S3 show the top-view morphology of SnO_2@VAG during different S-SCBD cycles. Notably, with the increase in the decorating cycle number, the SnO_2 amount on the VAG surface significantly increased. The SnO_2 nanoparticles did not agglomerate in only a specific part on the surface but rather uniformly and densely attached onto the surface of SnO_2@VAG-15 (Figure 2c−f). In particular, the SnO_2 nanoparticles in SnO_2@VAG-20 were decorated so much that they completely covered the edges and planes of the surface (Figure S3). The SnO_2 nanoparticles, which completely covered the VAG surface, induced aggregation between the particles inside the VAG electrodes, reducing the distance between the graphite layers from 40.88 to 26.04 μm. This led to a reduction in the accessible surface area where ion diffusion occurred. Moreover, it decreased the ionic conductivity of the surface, thereby reducing the electrical conductivity of the entire electrode.

Figures 3 and 4 show the characterization of SnO_2@VAG-15, TEM and HRTEM observations conducted to confirm the

https://doi.org/10.1021/acsomega.2c07075
ACS Omega 2023, 8, 6621−6631

crystallinity of the SnO_2 nanoparticles on the electrodes, and its morphology (Figure 3a). Numerous SnO_2 nanoparticles were formed on the graphene sheets from VAG. The average size of SnO_2 on VAG was approximately 4.16 ± 0.57 nm. The interlayer spacing between the SnO_2 nanoparticles was 0.32 nm, which corresponded to the (110) plane of SnO_2.[45] To further confirm the crystallinity of SnO_2@VAG-15, an XRD analysis was performed and compared with that of the VAG electrode. Figure 3b shows the XRD patterns of VAG (black line), SnO_2@VAG-15 (red line) prepared in this study, and SnO_2 obtained in accordance with the Joint Committee on Powder Diffraction Standards (JCPDS) file no. 41-1445 (blue pattern). In the XRD pattern of VAG, two peaks located at 2θ = 26.5° and 2θ = 54.5° corresponding to the (002) and (004) planes of graphite, respectively, can be observed.[46] It is estimated that the typical diffraction pattern of graphite is dominant in the XRD pattern of VAG since the anodization process oxidizes only the thin surface layer of VAG. On the other hand, the XRD pattern of SnO_2@VAG-15 exhibits various peaks at 2θ = 26.4, 33.7, 37.8, 51.6, 54.5, and 65.5° matching with the (110), (101), (200), (211), (220), and (301) planes of SnO_2, respectively.[47] These results suggest that SnO_2 decorated on the VAG electrode has a highly crystalline SnO_2 structure.

Chemical assessments, such as EDS, FT-IR, Raman, and XPS, were conducted to better understand the chemical binding state of the SnO_2 nanoparticles on the VAG surface. SnO_2 nanoparticles formed on VAG were composed of Sn and O, and the atomic contents of tin and oxygen were 36.27 and 63.26 at. %, respectively, showing a ratio of approximately 1:1.8 in the EDS measurement (Figure S4). The Raman and FT-IR spectra of SnO_2@VAG-15 show several peaks originating from the presence of SnO_2. Figure 3c shows the Raman spectra of VAG and SnO_2@VAG-15. Two peaks appear in the Raman spectrum of SnO_2@VAG-15 at 470.6 and 608.9 cm^{-1}, in addition to the D and G bands derived from VAG. These two peaks are derived from the asymmetric and symmetric stretching vibrations of Sn−O, respectively, and are the main peaks observed for SnO_2.[48] In addition to the absorption peaks caused by VAG, three new peaks can be observed in the FTIR spectrum of SnO_2@VAG-15 (Figure 3d). The absorption peaks located at 564 and 665 cm^{-1} could be attributed to the O−Sn−O and Sn−O stretching vibrations of SnO_2, respectively.[49] The absorption peaks simultaneously shown in the FT-IR spectra of VAG and SnO_2@VAG are attributed to the hydroxyl group (3440 cm^{-1}) and sp^2 carbon (1541, 1638 cm^{-1}) on the VAG surface.[50] The absorption peaks induced by C−H stretching (2849, 2918 cm^{-1}) are also observed. The peak at 1020 cm^{-1} is attributed to C−O stretching,[51] which seems to be due to the bonding of oxygen in SnO_2 and carbon on the VAG surface. These results support the finding that SnO_2 nanoparticles on VAG are composed of highly crystalline SnO_2 and suggest a favorable interfacial interaction between SnO_2 and the VAG surface.

Figure 4 shows the XPS survey spectrum and the O 1s and Sn 3d spectra of SnO_2@VAG-15. The XPS survey spectrum shows a Sn peak, and its oxygen content is approximately 62.34%, which is much higher than that of the VAG electrode (Figure 4a).[22] The oxygen content in the XPS survey spectrum is not consistent with the EDS result; as X-rays can penetrate only up to a nanometer depth during the analysis process, it was measured mainly on SnO_2 and part of the VAG surface. The O 1s XPS spectrum of SnO_2@VAG-15 can be deconvoluted into three components corresponding to the $O-Sn^{4+}$, $O-Sn^{2+}$, and C−O groups, the integrated peak intensity ratios of which are 62.01, 9.29, and 28.70%, respectively (Figure 4b). Because SnO_2 nanoparticles have a crystalline structure, the ratio of $O-Sn^{4+}$ groups is high. C−O groups were observed by combining the SnO_2 and VAG surfaces by annealing. $O-Sn^{2+}$ groups are most notable, typically observed in defective SnO_2 or SnO structures.[52] The Sn 3d peak was deconvoluted into two peaks corresponding to Sn^{4+} and Sn^{2+}, the integrated peak intensity ratios of which were 92.94 and 7.06%, respectively (Figure 4c). The Sn^{4+} peak is dominant in the Sn 3d spectrum; however, the Sn^{2+} peak also appears at a low ratio. This indicates that few defects existed inside the highly crystalline SnO_2 structure.

3.2. Electrochemical Performance of SnO_2@VAG. A three-cell test was conducted on the SnO_2-decorated VAG electrode to reveal the changes in the electrochemical characteristics with the progress of the cycles applied in the S-SCBD process. In this measurement, the potential range of the hybrid electrode was varied from 0 to 1 V, unlike that of the VAG electrode. The hybrid electrode showed stable curves in different ranges, not in the range of VAG. Figure 5a presents the CV curves of the VAG electrode and SnO_2@VAG for different S-SCBD cycles at a scanning rate of 200 mV s^{-1}. The CV curves of SnO_2@VAG exhibited a quasi-rectangular shape, similar to that of the VAG electrode. The intrinsic resistance (R_s) of SnO_2@VAG is estimated to be 0.761 Ω (Figure S5). This indicates that SnO_2@VAG has superior reversibility and low contact resistance in the electrode.[53,54] SnO_2@VAG had a higher current density range than the VAG electrodes. In particular, the current density range of SnO_2@VAG tended to increase slightly as the number of decorating cycles increased, indicating higher charging/discharging rates for SnO_2@VAG with higher decorating cycles.

Figure 5b shows the GCD curves of the VAG electrode and SnO_2@VAG for different S-SCBD cycles at a current density of 2 mA cm^{-2}. The GCD curves of SnO_2@VAG exhibited a quasi-symmetric triangular shape, indicating an excellent capacitive behavior. However, the curve shape of SnO_2@VAG is slightly different from that of the VAG electrode because the SnO_2 nanoparticles on VAG act like contact resistance. The calculated R_s of SnO_2@VAG (0.761 Ω) is larger than that of the VAG electrode (0.692 Ω, Figure S6). The areal capacitance of the hybrid electrode was calculated using the discharge time and current density (Figure 5b). Figure 5c shows the areal capacitance for different S-SCBD cycle numbers acquired at a current density of 2 mA cm^{-2}. The areal capacitance of the composite electrode tended to increase as the number of cycles increased. However, when the number of cycles exceeded 15, the area-specific capacitance decreased slightly. The reason why SnO_2@VAG exhibited the highest areal capacitance is as follows. As shown in the SEM images, numerous SnO_2 nanoparticles cover the entire surface of SnO_2@VAG, and these nanoparticles aggregate, resulting in a narrow gap between the adjacent graphite layers (Figure S3). In addition, many SnO_2 nanoparticles accumulated in the innermost part of the VAG electrode, reducing the accessible surface area (Figure S7). The amount of SnO_2 nanoparticles on SnO_2@VAG-20 affected the resistance of the electrode, thereby reducing the areal capacitance. The EIS data and the equivalent circuit of SnO_2@VAG-15 and 20 were obtained from the Nyquist plot to determine R_s of the electrode (Figure S5). The R_s values of SnO_2@VAG-15 and -20 were estimated

https://doi.org/10.1021/acsomega.2c07075
ACS Omega 2023, 8, 6621−6631

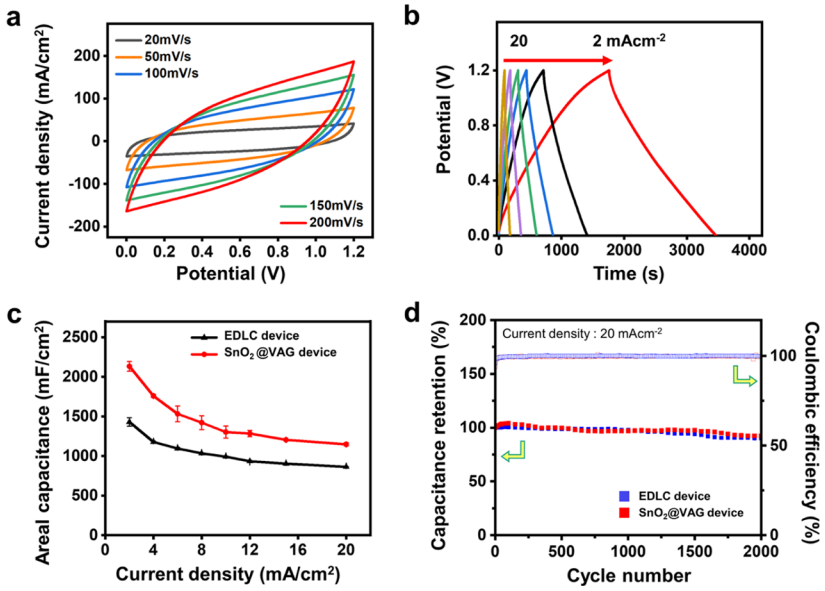

Figure 7. (a) CV curves of the supercapacitor device using SnO_2@VAG-15 at different scanning rates from 20 to 200 mV s^{-1}. (b) GCD curves of the supercapacitor device at different current densities from 2 to 20 mA cm^{-2}. (c) Variation of the areal capacitance of EDLC and supercapacitor devices by current densities. (d) Capacitance retention and Coulombic efficiency of EDLC and supercapacitor device after 2000 cycles.

to be 0.761 and 0.837 Ω, respectively. This indicates that the resistance of the electrode increased with the increasing amount of SnO_2 on the surface. An increased electrode resistance lowers the areal capacitance and ion transfer in the electrode.[55] Consequently, the areal capacitance of SnO_2@VAG-20 decreased owing to the reduced surface area and increased resistance.

The electrochemical characteristics of SnO_2@VAG-15 were investigated in detail. Figure 5d shows the CV curves of SnO_2@VAG-15 acquired at scanning rates ranging from 20 to 200 mV s^{-1}. The current density of the electrode with an increasing scanning rate was similar to that observed for typical EDLCs. The GCD curves of SnO_2@VAG-15 showed a quasi-symmetric triangular shape, regardless of the current density (Figure 5e). The areal capacitance of SnO_2@VAG-15 was plotted with respect to the current density using the discharging time in the GCD curves, which were compared with those of the VAG electrode (Figure 5f). SnO_2@VAG-15 showed a significantly higher area-specific capacitance than the VAG electrode at the same current density. In particular, when the current density was 2 mA cm^{-2}, the areal capacitance of SnO_2@VAG-15 was 4402 mF cm^{-2}, which was approximately 58% higher than that of the VAG electrode. The volumetric capacitance of SnO_2@VAG was 9.57 F cm^{-2}. The areal and volumetric capacitance values of SnO_2@VAG are much higher than those of a hybrid electrode using SnO_2.[56] The outstanding electrochemical performance of SnO_2@VAG was attributed to its morphology and the synergistic effect between graphene and SnO_2. Nano-sized SnO_2 particles on VAG exhibited excellent stability and higher ion diffusion rates to support charge transfer.[57] In addition, the SnO_2 nanoparticles attached onto the VAG surface increased the surface area of the electrode (Figure 2d,f). In particular, the contact area between SnO_2 and graphene increased significantly owing to the vertical structure, thereby enhancing the synergistic effect between the two materials.[58] Therefore, the electrochemical performance of SnO_2@VAG was significantly improved compared with that of the VAG electrode. However, the degree of improvement in the areal capacitance of SnO_2@VAG-15 decreased with the increasing current density. At a current density of 20 $mAcm^{-2}$, the areal capacitance of SnO_2@VAG-15 was 2,580 mF cm^{-2}, which was approximately 11% higher than that of the VAG electrode. These results can be attributed to the insufficient ion transfer at a high current density owing to the valley structure of the electrode.

To investigate the effect of the sonication process on the electrochemical performance of SnO_2@VAG, a three-cell test was conducted on the SnO_2@VAG-15 synthesized with sonication (SnO_2@VAG-15 w soni) and without sonication (SnO_2@VAG-15 w/o soni) during the S-SCBD process (Figure 6). Figure 6a presents the CV curves of the SnO_2@VAG-15 synthesized with sonication and without sonication during the S-SCBD process at a scanning rate of 200 mV s^{-1}. SnO_2@VAG-15 w/o soni shows a current density range from −50.36 to 54.68 mA/cm^2, which is much lower than that of the SnO_2@VAG-15 w soni. The discharging time of the SnO_2@VAG-15 w/o soni is lower than that of the SnO_2@VAG-15 w soni, resulting in a poor areal capacitance of 830.72 mF/cm^2 (Figure 6b). The difference in electrochemical performance according to the presence of the sonication process is attributed to the agglomeration of SnO_2 nanoparticles at the edges of the VAG electrode. In the SnO_2@VAG-15 w/o soni, the SnO_2 nanoparticles densely formed at the edge of the VAG are aggregated with the other SnO_2 nanoparticles formed in the adjacent graphite layer, thereby significantly reducing the gap between the adjacent graphite layers (Figure 2b). As a result, the electrolyte ion cannot penetrate smoothly into the surface inside the VAG inlet, reducing practical SSA. The decrease in SSA hinders the areal capacitance of the SnO2@VAG-15 w/o soni. These results suggest that the sonication process during the sequential CBD method is one of the decisive factors in improving the areal capacitance of SnO_2@VAG.

3.3. Electrochemical Performance of the Supercapacitor Device. A supercapacitor device was manufactured using two pieces of SnO_2@VAG-15 (Figure S8), and the

https://doi.org/10.1021/acsomega.2c07075
ACS Omega 2023, 8, 6621−6631

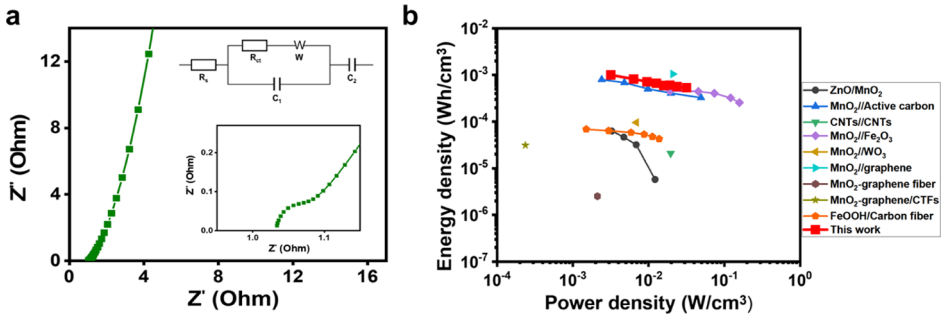

Figure 8. (a) Nyquist plot and electrical equivalent circuit (inset) of the supercapacitor devices. (b) Energy and power density comparison of the supercapacitor device using SnO_2@VAG-15 and other hybrid electrodes.

electrochemical characteristics of the device were evaluated. An EDLC was fabricated using the same process and material. Figure 7a shows the CV curves of the supercapacitor device acquired at various scanning rates. The CV curve of the supercapacitor has a quasi-rectangular shape, similar to that of the three-electrode test system. Furthermore, the CV curve of the supercapacitor exhibited a much higher current density than that of the EDLC (Figure S9). The current density of the supercapacitor ranged from −164 to 187 mA cm^{-2}, whereas that of the EDLC ranged from −84 to 97 mA cm^{-2}. Figure 7b shows the GCD curves of the supercapacitor acquired at various current densities. The GCD curves of the supercapacitor had a quasi-symmetric triangular shape, indicating a smooth charging and discharging process. The areal capacitances of the supercapacitor and EDLC based on the current density were calculated and plotted (Figure 7c). The supercapacitor exhibited a higher areal capacitance than the EDLC at all current densities. The areal capacitance of the supercapacitor at a current density of 2 mA cm^{-2} was 2132 mF cm^{-2}, which was approximately 49% higher than that of the EDLC. These results suggest that the supercapacitor exhibited excellent ion-transfer rates and areal capacitance. The areal capacitance retention and Coulombic efficiency of the hybrid device were measured to determine the cyclic stability of the device after long-term use (Figure 7d). The capacitance retention of the supercapacitor was calculated by dividing the areal capacitance at a specific cycle with that obtained at the first cycles, and the Coulombic efficiency was determined by the ratio of the discharging capacitance to the charging capacitance.[59] The supercapacitor device exhibited a capacitance retention of 90% after 2000 cycles of repeated charge/discharge processes; this value was similar to that of the EDLC. Moreover, the Coulombic efficiency of the supercapacitor was maintained at approximately 100% after 2000 cycles, indicating a smooth charging/discharging process. These results indicate the outstanding cyclic stability of the supercapacitor. The interface interaction between graphene and SnO_2 in a large contact area supplements the poor cycle stability of the SnO_2 nanoparticles, resulting in stable capacitance retention even after long cycles.[60]

The equivalent circuit of the supercapacitor was drawn using a fitted Nyquist plot obtained from the EIS data, and the resistance values were calculated using the equivalent circuit (Figure 8a). In the equivalent circuit, the R_s and R_{ct} values of the supercapacitor were estimated to be 1.036 and 0.089 Ω, respectively, which are low. The low resistance of the supercapacitor can be attributed to the superior interfacial interaction between SnO_2 and graphene.[54]

The energy and power densities of the fabricated supercapacitor were calculated and compared with those of the devices with other hybrid electrodes (Figure 8b). The fabricated supercapacitor shows the superior power densities of 3.17−31.74 mW cm^{-3} and energy densities of 0.53−0.93 mW h cm^{-3}. SnO_2@VAG has a higher energy density than MO/graphene electrodes.[61] The power densities of SnO_2@VAG were also more favorable than those of the other devices. This is because of the synergistic effect between graphene and SnO_2, and the large surface area of the hybrid electrode. These results suggest that the fabricated supercapacitor using SnO_2@VAG demonstrates a superior electrochemical performance and outstanding cyclic stability when compared with other supercapacitor devices. Therefore, the preparation of the hybrid electrodes using the ultrasonication-assisted method can greatly improve the performance of the supercapacitor.

4. CONCLUSIONS

In summary, we developed a facile method for fabricating hybrid electrodes with excellent areal capacitance and cyclic stability and verified its applicability. Hybrid electrodes uniformly decorated with SnO_2 nanoparticles on a VAG surface were prepared using the S-SCBD method. The sonication treatment applied during the MO decoration process allowed the precursor solution to reach the interior regions of the surface owing to the cavitation effect. Furthermore, it promoted MO nucleation on the entire VAG surface. Thus, numerous small and homogeneous SnO_2 nanoparticles were uniformly attached onto the entire surface of the VAG electrode after S-SCBD. With the increase in the number of S-SCBD cycles, the VAG surface saw more SnO_2 nanoparticles. SnO_2@VAG exhibited an outstanding areal capacitance (4.40 F cm^{-2}), up to 58% higher than that of VAG electrodes. Furthermore, the areal capacitance of SnO_2@VAG is higher than that of SnO_2@VAG without the sonication process by a factor of 5.30. The supercapacitor with SnO_2@VAG showed an excellent areal capacitance (2.13 F cm^{-2}) and a cyclic stability of 90% after 2000 cycles. SnO_2@VAG was produced through a single process using a few nonharmful chemicals, and the sonication process improved the areal capacitance of the VAG-based hybrid electrode. Our approach is expected to be highly useful in the energy-storage industry, which requires an eco-friendly system.

■ ASSOCIATED CONTENT

Supporting Information

The Supporting Information is available free of charge at https://pubs.acs.org/doi/10.1021/acsomega.2c07075.

https://doi.org/10.1021/acsomega.2c07075
ACS Omega 2023, 8, 6621−6631

FE-SEM images of the top-view morphology of SnO_2@VAG-5, SnO_2@VAG-10, and SnO_2@VAG-20; EDS spectrum of SnO_2@VAG-15 with its atomic percent; Nyquist plot of SnO_2@VAG-15 and -20; top-view and side-view morphologies of SnO_2@VAG-15 and -20; Nyquist plot of the VAG electrodes; architecture of the symmetric supercapacitor using two pieces of SnO_2@VAG-15; and CV curves of the EDLC and supercapacitor device acquired at 200 mV s^{-1} (PDF)

AUTHOR INFORMATION

Corresponding Author

Sung Oh Cho − *Department of Nuclear and Quantum Engineering, Korea Advanced Institute of Science and Technology (KAIST), 34141 Daejeon, Republic of Korea;* orcid.org/0000-0002-5441-3244; Phone: +82-42-350-3823; Email: socho@kaist.ac.kr

Authors

Na Eun Lee − *Department of Nuclear and Quantum Engineering, Korea Advanced Institute of Science and Technology (KAIST), 34141 Daejeon, Republic of Korea*

Seung Uk Cheon − *Department of Nuclear and Quantum Engineering, Korea Advanced Institute of Science and Technology (KAIST), 34141 Daejeon, Republic of Korea*

Jaewoo Lee − *Department of Nuclear and Quantum Engineering, Korea Advanced Institute of Science and Technology (KAIST), 34141 Daejeon, Republic of Korea;* orcid.org/0000-0002-3576-5324

Complete contact information is available at: https://pubs.acs.org/10.1021/acsomega.2c07075

Author Contributions

The manuscript was written through contributions of all authors. All authors have given approval to the final version of the manuscript.

Funding

This work was supported by the National Research Foundation of Korea (NRF) grant funded by the Korea government (NRF-2020M2D8A2069727) and Ministry of Science and ICT of Korea (2022M2E9A3048435).

Notes

The authors declare no competing financial interest.

ACKNOWLEDGMENTS

This work was supported by the National Research Foundation of Korea (NRF) grant funded by the Korean government (NRF-2020M2D8A2069727) and Ministry of Science and ICT of Korea (2022M2E9A3048435).

ABBREVIATIONS

VAG, vertically aligned graphene; SnO_2, tin oxide; SnO2@VAG, SnO_2 nanoparticle-decorated VAG electrodes; S-SCBD, sonication-assisted sequential chemical bath deposition; EDLCs, electric double-layer capacitors; SSA, specific surface area; MOs, metal oxides; CBD, chemical bath deposition; GF, graphite foil; FE-SEM, field-emission scanning electron microscopy; HRTEM, high-resolution transmission electron microscopy; XPS, X-ray photoelectron spectroscopy; CV, cyclic voltammetry; GCD, galvanostatic charging/discharging; EIS, electrochemical impedance spectroscopy; GO, graphene oxide; SCE, standard calomel electrode

REFERENCES

(1) Wang, Y.; Zhang, L.; Hou, H.; Xu, W.; Duan, G.; He, S.; Liu, K.; Jiang, S. Recent progress in carbon-based materials for supercapacitor electrodes: a review. *J. Mater. Sci.* **2021**, *56*, 173−200.

(2) (a) Zhang, Y.; Zeng, T.; Huang, D.; Yan, W.; Zhang, Y.; Wan, Q.; Yang, N. High-energy-density supercapacitors from dual pseudocapacitive nanoelectrodes. *ACS Appl. Energy Mater.* **2020**, *3*, 10685−10694. (b) Ghosh, K.; Srivastava, S. K. Enhanced supercapacitor performance and electromagnetic interference shielding effectiveness of CuS quantum dots grown on reduced graphene oxide sheets. *ACS Omega* **2021**, *6*, 4582−4596. (c) Arunachalam, S.; Kirubasankar, B.; Pan, D.; Liu, H.; Yan, C.; Guo, Z.; Angaiah, S. Research progress in rare earths and their composites based electrode materials for supercapacitors. *Green Energy Environ.* **2020**, *5*, 259−273.

(3) Sankar, K. V.; Selvan, R. K. The ternary MnFe2O4/graphene/polyaniline hybrid composite as negative electrode for supercapacitors. *J. Power Sources* **2015**, *275*, 399−407.

(4) Zhang, Y.; Wang, C.; Chen, X.; Dong, X.; Meng, C.; Huang, C. Bamboo leaves as sustainable sources for the preparation of amorphous carbon/iron silicate anode and nickel−cobalt silicate cathode materials for hybrid Supercapacitors. *ACS Appl. Energy Mater.* **2021**, *4*, 9328−9340.

(5) Liu, X.; Zou, S.; Liu, K.; Lv, C.; Wu, Z.; Yin, Y.; Liang, T.; Xie, Z. Highly compressible three-dimensional graphene hydrogel for foldable all-solid-state supercapacitor. *J. Power Sources* **2018**, *384*, 214−222.

(6) (a) Bose, S.; Kuila, T.; Mishra, A. K.; Rajasekar, R.; Kim, N. H.; Lee, J. H. Carbon-based nanostructured materials and their composites as supercapacitor electrodes. *J. Mater. Chem.* **2012**, *22*, 767−784. (b) Bazan-Aguilar, A.; Ponce-Vargas, M.; Caycho, C. L.; La Rosa-Toro, A.; Baena-Moncada, A. M. Highly porous reduced graphene oxide-coated carbonized cotton fibers as supercapacitor electrodes. *ACS Omega* **2020**, *5*, 32149−32159.

(7) (a) Ke, Q.; Wang, J. Graphene-based materials for supercapacitor electrodes - A review. *J. Materiomics* **2016**, *2*, 37−54. (b) Bokhari, S. W.; Siddique, A. H.; Sherrell, P. C.; Yue, X.; Karumbaiah, K. M.; Wei, S.; Ellis, A. V.; Gao, W. Advances in graphene-based supercapacitor electrodes. *Energy Rep.* **2020**, *6*, 2768−2784.

(8) VahidMohammadi, A.; Mojtabavi, M.; Caffrey, N. M.; Wanunu, M.; Beidaghi, M. Assembling 2D MXenes into highly stable pseudocapacitive electrodes with high power and energy densities. *Adv. Mater.* **2019**, *31*, 1806931.

(9) (a) Boota, M.; Bécuwe, M.; Gogotsi, Y. Phenothiazine-MXene Aqueous Asymmetric Pseudocapacitors. *ACS Appl. Energy Mater.* **2020**, *3*, 3144−3149. (b) Tyagi, A.; Joshi, M. C.; Shah, A.; Thakur, V. K.; Gupta, R. K. Hydrothermally Tailored Three-Dimensional Ni-V Layered Double Hydroxide Nanosheets as High-Performance Hybrid Supercapacitor Applications. *ACS Omega* **2019**, *4*, 3257−3267.

(10) Muzaffar, A.; Ahamed, M. B.; Deshmukh, K.; Thirumalai, J. A review on recent advances in hybrid supercapacitors: Design, fabrication and applications. *Renewable Sustainable Energy Rev.* **2019**, *101*, 123−145.

(11) Shown, I.; Ganguly, A.; Chen, L. C.; Chen, K. H. Conducting polymer-based flexible supercapacitor. *Energy Sci. Eng.* **2015**, *3*, 2−26.

(12) Sun, B.; Zhang, X.; Fan, X.; Wang, R.; Bai, H.; Wei, X. Interface modification based on MnO2@N-doped activated carbon composites for flexible solid-state asymmetric supercapacitors. *Energy* **2022**, *249*, 123659.

(13) Velmurugan, V.; Srinivasarao, U.; Ramachandran, R.; Saranya, M.; Grace, A. N. Synthesis of tin oxide/graphene (SnO2/G) nanocomposite and its electrochemical properties for supercapacitor applications. *Mater. Res. Bull.* **2016**, *84*, 145−151.

(14) Jin, X.; Wang, H.; Liu, Y.; Wang, H.; Wang, W.; Lin, T. Hydrogen-bonding power interfacial load transfer of carbon fabric/polypyrrole composite pseudosupercapacitor electrode with improved electrochemical stability. *Appl. Surf. Sci.* **2019**, *470*, 783−791.

(15) (a) Yaqoob, A. A.; Mohd Noor, M.; Serrà, A.; Mohamad Ibrahim, M. N. Advances and challenges in developing efficient graphene oxide-based ZnO photocatalysts for dye photo-oxidation. *Nanomaterials* **2020**, *10*, 932. (b) Kirubasankar, B.; Balan, B.; Yan, C.; Angaiah, S. Recent Progress in Graphene-Based Microsupercapacitors. *Energy Technol.* **2021**, *9*, 2000844.
(16) (a) Liu, Y.; Zeng, Z.; Wei, J. Frontiers in nano-architectured carbon−metal oxide electrodes for supercapacitance energy storage: a review. *Frontiers Nanosci. Nanotechnol.* **2016**, *2*, 78. (b) Keshari, A. S.; Dubey, P. Rapid microwave-assisted vs. hydrothermal synthesis of hierarchical sheet-like NiO/NiMoO4 hybrid nanostructures for high performance extrinsic pseudocapacitor application. *J. Energy Storage* **2021**, *40*, 102629.
(17) Madhu, R.; Dinesh, B.; Chen, S.-M.; Saraswathi, R.; Mani, V. An electrochemical synthesis strategy for composite based ZnO microspheres−Au nanoparticles on reduced graphene oxide for the sensitive detection of hydrazine in water samples. *RSC Adv.* **2015**, *5*, 54379−54386.
(18) (a) Wang, W.; Lu, L.; Xie, Y.; Mei, X.; Tang, Y.; Wu, W.; Liang, R. Tailoring the surface morphology and nanoparticle distribution of laser-induced graphene/Co3O4 for high-performance flexible micro-supercapacitors. *Appl. Surf. Sci.* **2020**, *504*, 144487. (b) Liu, H.; Moon, K.-s.; Li, J.; Xie, Y.; Liu, J.; Sun, Z.; Lu, L.; Tang, Y.; Wong, C.-P. Laser-oxidized Fe3O4 nanoparticles anchored on 3D macroporous graphene flexible electrodes for ultrahigh-energy in-plane hybrid micro-supercapacitors. *Nano Energy* **2020**, *77*, 105058.
(19) Dhara, A.; Hodes, G.; Sarkar, S. K. Two stage chemical bath deposition of MoO 3 nanorod films. *RSC Adv.* **2014**, *4*, 53694−53700.
(20) (a) Islam, S.; Mia, M. M.; Shah, S. S.; Naher, S.; Shaikh, M. N.; Aziz, M. A.; Ahammad, A. S. Recent Advancements in Electrochemical Deposition of Metal-Based Electrode Materials for Electrochemical Supercapacitors. *Chem. Rec.* **2022**, *22*, No. e202200013. (b) Liu, H.; Sun, Z.; Chen, Y.; Zhang, W.; Chen, X.; Wong, C.-P. Laser Processing of Flexible In-Plane Micro-supercapacitors: Progresses in Advanced Manufacturing of Nanostructured Electrodes. *ACS Nano* **2022**, *16*, 10088−10129.
(21) Alhebshi, N. A.; Rakhi, R.; Alshareef, H. N. Conformal coating of Ni (OH) 2 nanoflakes on carbon fibers by chemical bath deposition for efficient supercapacitor electrodes. *J. Mater. Chem. A* **2013**, *1*, 14897−14903.
(22) Lee, N. E.; Lee, J.; Jeong, H. Y.; Lee, S. Y.; Cho, S. O. Vertically aligned graphene prepared by the electrochemical anodization of graphite foil for supercapacitor electrodes. *J. Power Sources* **2022**, *526*, 231137.
(23) (a) Li, J.; Östling, M. Prevention of graphene restacking for performance boost of supercapacitors—a review. *Crystals* **2013**, *3*, 163−190. (b) Liao, Q.; Li, S.; Cui, H.; Wang, C. Vertically-aligned graphene@ Mn 3 O 4 nanosheets for a high-performance flexible all-solid-state symmetric supercapacitor. *J. Mater. Chem. A* **2016**, *4*, 8830−8836.
(24) Han, Z. J.; Pineda, S.; Murdock, A. T.; Seo, D. H.; Ostrikov, K. K.; Bendavid, A. RuO 2-coated vertical graphene hybrid electrodes for high-performance solid-state supercapacitors. *J. Mater. Chem. A* **2017**, *5*, 17293−17301.
(25) Xie, Y.; Ali, G.; Yoo, S. H.; Cho, S. O. Sonication-assisted synthesis of CdS quantum-dot-sensitized TiO2 nanotube arrays with enhanced photoelectrochemical and photocatalytic activity. *ACS Appl. Mater. Interfaces* **2010**, *2*, 2910−2914.
(26) Khaliq, N.; Rasheed, M. A.; Khan, M.; Maqbool, M.; Ahmad, M.; Karim, S.; Nisar, A.; Schmuki, P.; Cho, S. O.; Ali, G. Voltage-switchable biosensor with gold nanoparticles on TiO2 nanotubes decorated with CdS quantum dots for the detection of cholesterol and H2O2. *ACS Appl. Mater. Interfaces* **2021**, *13*, 3653−3668.
(27) Shchukin, D. G.; Skorb, E.; Belova, V.; Möhwald, H. Ultrasonic cavitation at solid surfaces. *Adv. Mater.* **2011**, *23*, 1922−1934.
(28) Hamida, T.; Babadagli, T. Effects of ultrasonic waves on the interfacial forces between oil and water. *Ultrason. Sonochem.* **2008**, *15*, 274−278.
(29) Choudhury, B. J.; Roy, K.; Moholkar, V. S. Improvement of supercapacitor performance through enhanced interfacial interactions induced by sonication. *Ind. Eng. Chem. Res.* **2021**, *60*, 7611−7623.
(30) (a) Oliva, A.; Castro-Rodrıguez, R.; Solıs-Canto, O.; Sosa, V. c.; Quintana, P.; Pena, J. Comparison of properties of CdS thin films grown by two techniques. *Appl. Surf. Sci.* **2003**, *205*, 56−64. (b) Choi, J. Y.; Kim, K.-J.; Yoo, J.-B.; Kim, D. Properties of cadmium sulfide thin films deposited by chemical bath deposition with ultrasonication. *Sol. Energy* **1998**, *64*, 41−47.
(31) Ma, H.; Kong, D.; Xu, Y.; Xie, X.; Tao, Y.; Xiao, Z.; Lv, W.; Jang, H. D.; Huang, J.; Yang, Q. H. Disassembly−reassembly approach to RuO2/graphene composites for ultrahigh volumetric capacitance supercapacitor. *Small* **2017**, *13*, 1701026.
(32) Zhou, H.; Yang, X.; Lv, J.; Dang, Q.; Kang, L.; Lei, Z.; Yang, Z.; Hao, Z.; Liu, Z.-H. Graphene/MnO2 hybrid film with high capacitive performance. *Electrochim. Acta* **2015**, *154*, 300−307.
(33) Sethi, M.; Shenoy, U. S.; Bhat, D. K. Simple solvothermal synthesis of porous graphene-NiO nanocomposites with high cyclic stability for supercapacitor application. *J. Alloys Compd.* **2021**, *854*, 157190.
(34) Liao, Q.; Li, N.; Jin, S.; Yang, G.; Wang, C. All-solid-state symmetric supercapacitor based on Co3O4 nanoparticles on vertically aligned graphene. *ACS Nano* **2015**, *9*, 5310−5317.
(35) Kirubasankar, B.; Murugadoss, V.; Lin, J.; Ding, T.; Dong, M.; Liu, H.; Zhang, J.; Li, T.; Wang, N.; Guo, Z.; Angaiah, S. In situ grown nickel selenide on graphene nanohybrid electrodes for high energy density asymmetric supercapacitors. *Nanoscale* **2018**, *10*, 20414−20425.
(36) Kirubasankar, B.; Narayanasamy, M.; Yang, J.; Han, M.; Zhu, W.; Su, Y.; Angaiah, S.; Yan, C. Construction of heterogeneous 2D layered MoS2/MXene nanohybrid anode material via interstratification process and its synergetic effect for asymmetric supercapacitors. *Appl. Surf. Sci.* **2020**, *534*, 147644.
(37) Jayaweera, V.; Liyanage, W.; Silva, R.; Rosa, S.; Kottegoda, I. Reduced Graphene Oxide-SnO2-Polyaniline Ternary Composite for High-Performance Supercapacitors. *Mater. Sci. Res. India* **2021**, *18*, 206−216.
(38) Ramesh, S.; Yadav, H.; Lee, Y.-J.; Hong, G.-W.; Kathalingam, A.; Sivasamy, A.; Kim, H.-S.; Kim, H. S.; Kim, J.-H. Porous materials of nitrogen doped graphene oxide@ SnO2 electrode for capable supercapacitor application. *Sci. Rep.* **2019**, *9*, 12622.
(39) Chen, J.; Zhu, T.; Fu, X.; Ren, G.; Wang, C. Constructing ultrafine tin dioxide/few-walled carbon nanotube composites for high-performance supercapacitors. *Int. J. Electrochem. Sci.* **2019**, *14*, 7293−7302.
(40) Wang, W.; Li, Y.; Li, L.; Wang, L.; Wang, K. SnO2/TiO2 nanocomposite prepared by pulsed laser deposition as anode material for flexible quasi-solid-state lithium-ion batteries. *Int. J. Electrochem. Sci.* **2020**, *15*, 11709−11722.
(41) (a) Min, X.; Sun, B.; Chen, S.; Fang, M.; Wu, X.; Liu, Y. g.; Abdelkader, A.; Huang, Z.; Liu, T.; Xi, K.; Vasant Kumar, R. A textile-based SnO2 ultra-flexible electrode for lithium-ion batteries. *Energy Storage Mater.* **2019**, *16*, 597−606. (b) Asen, P.; Haghighi, M.; Shahrokhian, S.; Taghavinia, N. One step synthesis of SnS2-SnO2 nano-heterostructured as an electrode material for supercapacitor applications. *J. Alloys Compd.* **2019**, *782*, 38−50.
(42) Sephra, P. J.; Baraneedharan, P.; Sivakumar, M.; Thangadurai, T. D.; Nehru, K. Size controlled synthesis of SnO2 and its electrostatic self-assembly over reduced graphene oxide for photocatalyst and supercapacitor application. *Mater. Res. Bull.* **2018**, *106*, 103−112.
(43) (a) Paul, A.; Ghosh, S.; Kolya, H.; Kang, C.-W.; Murmu, N. C.; Kuila, T. High performance asymmetric supercapacitor device based on lanthanum doped nickel-tin oxide/reduced graphene oxide composite. *J. Energy Storage* **2022**, *55*, 105526. (b) Kumar, R.; Nekouei, R. K.; Sahajwalla, V. In-situ carbon-coated tin oxide (ISCC-SnO2) for micro-supercapacitor applications. *Carbon Lett.* **2020**, *30*, 699−707. (c) Kim, T.; Samuel, E. P.; Park, C.; Kim, Y.-I.; Aldalbahi, A.; Alotaibi, F.; Yoon, S. S. Wearable fabric supercapacitors using

https://doi.org/10.1021/acsomega.2c07075
ACS Omega 2023, 8, 6621−6631

supersonically sprayed reduced graphene and tin oxide. *J. Alloys Compd.* **2021**, *856*, 157902.
(44) Kumar, P.; Rao, G. K. The effect of precursor concentration and post-deposition annealing on the optical and micro-structural properties of SILAR deposited SnO2 films. *Mater. Res. Express* **2020**, *7*, 016428.
(45) (a) Liu, W.; Yin, K.; He, F.; Ru, Q.; Zuo, S.; Yao, C. A highly efficient reduced graphene oxide/SnO2/TiO2 composite as photo-anode for photocathodic protection of 304 stainless steel. *Mater. Res. Bull.* **2019**, *113*, 6−13. (b) Mishra, R.; Upadhyay, S.; Kushwaha, A.; Kim, T.-H.; Murali, G.; Verma, R.; Srivastava, M.; Singh, J.; Sahay, P.; Hee Lee, S. H. SnO 2 quantum dots decorated on RGO: A superior sensitive, selective and reproducible performance for a H 2 and LPG sensor. *Nanoscale* **2015**, *7*, 11971−11979.
(46) Ain, Q. T.; Haq, S. H.; Alshammari, A.; Al-Mutlaq, M. A.; Anjum, M. N. The systemic effect of PEG-nGO-induced oxidative stress in vivo in a rodent model. *Beilstein J. Nanotechnol.* **2019**, *10*, 901−911.
(47) Debataraja, A.; Zulhendri, D. W.; Yuliarto, B.; Nugraha, B.; Hiskia; Sunendar, B. Investigation of nanostructured SnO2 synthesized with polyol technique for CO gas sensor applications. *Procedia Eng.* **2017**, *170*, 60−64.
(48) Naresh, N.; Narsimulu, D.; Jena, P.; Srinadhu, E.; Satyanarayana, N. Microwave-assisted hydrothermal synthesis of SnO2/reduced graphene-oxide nanocomposite as anode material for high performance lithium-ion batteries. *J. Mater. Sci.: Mater. Electron.* **2018**, *29*, 14723−14732.
(49) Paramarta, V.; Taufik, A.; Saleh, R. Better Adsorption Capacity of SnO_2 Nanoparticles with Different Graphene Addition. 8th International Conference on Physics and Its Applications (ICOPIA); *Journal of Physics: Conference Series*; IOP Publishing, 2016; Vol. *776*, p 012039.
(50) Lee, N. E.; Jeong, J.-M.; Lim, H.; Lee, S. Y.; Cho, S. O. Ultraviolet/blue light emitting high-quality graphene quantum dots and their biocompatibility. *Carbon* **2020**, *170*, 213−219.
(51) Verma, S.; Verma, B. Synthesis of sulfur/phosphorous-doped graphene aerogel as a modified super capacitor electrode. *Int. J. Chem. Stud.* **2018**, *6*, 111−117.
(52) Nagata, T.; Bierwagen, O.; White, M. E.; Tsai, M.-Y.; Speck, J. S. Study of the Au Schottky contact formation on oxygen plasma treated n-type SnO2 (101) thin films. *J. Appl. Phys.* **2010**, *107*, 033707.
(53) Lee, J. H.; Chae, J. S.; Jeong, J. H.; Ahn, H.-J.; Roh, K. C. An ionic liquid incorporated in a quasi-solid-state electrolyte for high-temperature supercapacitor applications. *Chem. Commun.* **2019**, *55*, 15081−15084.
(54) Cheng, Q.; Tang, J.; Ma, J.; Zhang, H.; Shinya, N.; Qin, L.-C. Graphene and nanostructured MnO2 composite electrodes for supercapacitors. *Carbon* **2011**, *49*, 2917−2925.
(55) Senthilkumar, S.; Selvan, R. K.; Lee, Y.; Melo, J. Electric double layer capacitor and its improved specific capacitance using redox additive electrolyte. *J. Mater. Chem. A* **2013**, *1*, 1086−1095.
(56) (a) Chang, J.-H.; Lin, M.-F.; Kuo, Y.-L.; Yang, C.-R.; Chen, J.-Z. Flexible rGO-SnO2 supercapacitors converted from pastes containing SnCl2 liquid precursor using atmospheric-pressure plasma jet. *Ceram. Int.* **2021**, *47*, 1651−1659. (b) Shah, S. S.; Aziz, M. A.; Al-Betar, A.-R.; Mahfoz, W. Electrodeposition of polyaniline on high electroactive indium tin oxide nanoparticles-modified fluorine doped tin oxide electrode for fabrication of high-performance hybrid supercapacitor. *Arabian J. Chem.* **2022**, *15*, 104058. (c) Bian, H.; Tian, Y.; Lee, C.; Yuen, M.-F.; Zhang, W.; Li, Y. Y. Mesoporous SnO2 nanostructures of ultrahigh surface areas by novel anodization. *ACS Appl. Mater. Interfaces* **2016**, *8*, 28862−28871.
(57) Bonu, V.; Gupta, B.; Chandra, S.; Das, A.; Dhara, S.; Tyagi, A. Electrochemical supercapacitor performance of SnO2 quantum dots. *Electrochim. Acta* **2016**, *203*, 230−237.
(58) Jiang, H.; Ma, J.; Li, C. *Mesoporous Carbon Incorporated Metal Oxide Nanomaterials as Supercapacitor Electrodes*; Wiley Online Library, 2012.
(59) (a) Chang, T.-W.; Lin, L.-Y.; Peng, P.-W.; Zhang, Y. X.; Huang, Y.-Y. Enhanced electrocapacitive performance for the supercapacitor with tube-like polyaniline and graphene oxide composites. *Electrochim. Acta* **2018**, *259*, 348−354. (b) Rajkumar, M.; Hsu, C.-T.; Wu, T.-H.; Chen, M.-G.; Hu, C.-C. Advanced materials for aqueous supercapacitors in the asymmetric design. *Prog. Nat. Sci.: Mater. Int.* **2015**, *25*, 527−544.
(60) Zhi, M.; Xiang, C.; Li, J.; Li, M.; Wu, N. Nanostructured carbon-metal oxide composite electrodes for supercapacitors: a review. *Nanoscale* **2013**, *5*, 72−88.
(61) (a) Yao, B.; Huang, L.; Zhang, J.; Gao, X.; Wu, J.; Cheng, Y.; Xiao, X.; Wang, B.; Li, Y.; Zhou, J. Flexible transparent molybdenum trioxide nanopaper for energy storage. *Adv. Mater.* **2016**, *28*, 6353−6358. (b) Yang, P.; Xiao, X.; Li, Y.; Ding, Y.; Qiang, P.; Tan, X.; Mai, W.; Lin, Z.; Wu, W.; Li, T.; Jin, H.; Liu, P.; Zhou, J.; Wong, C. P.; Wang, Z. L. Hydrogenated ZnO core−shell nanocables for flexible supercapacitors and self-powered systems. *ACS Nano* **2013**, *7*, 2617−2626. (c) Zuo, W.; Xie, C.; Xu, P.; Li, Y.; Liu, J. A Novel Phase-Transformation Activation Process toward Ni-Mn-O Nanoprism Arrays for 2.4 V Ultrahigh-Voltage Aqueous Supercapacitors. *Adv. Mater.* **2017**, *29*, 1703463. (d) Zhang, L.; Zhu, P.; Zhou, F.; Zeng, W.; Su, H.; Li, G.; Gao, J.; Sun, R.; Wong, C.-p. Flexible asymmetrical solid-state supercapacitors based on laboratory filter paper. *ACS Nano* **2016**, *10*, 1273−1282. (e) Kaempgen, M.; Chan, C. K.; Ma, J.; Cui, Y.; Gruner, G. Printable thin film supercapacitors using single-walled carbon nanotubes. *Nano Lett.* **2009**, *9*, 1872−1876. (f) Lu, X.; Zeng, Y.; Yu, M.; Zhai, T.; Liang, C.; Xie, S.; Balogun, M. S.; Tong, Y. Oxygen-deficient hematite nanorods as high-performance and novel negative electrodes for flexible asymmetric supercapacitors. *Adv. Mater.* **2014**, *26*, 3148−3155. (g) Lyu, L.; Seong, K.-d.; Kim, J. M.; Zhang, W.; Jin, X.; Kim, D. K.; Jeon, Y.; Kang, J.; Piao, Y. CNT/high mass loading MnO2/graphene-grafted carbon cloth electrodes for high-energy asymmetric supercapacitors. *Nano-Micro Lett.* **2019**, *11*, 88. (h) Ji, S.-H.; Chodankar, N. R.; Jang, W.-S.; Kim, D.-H. High mass loading of h-WO3 and α-MnO2 on flexible carbon cloth for high-energy aqueous asymmetric supercapacitor. *Electrochim. Acta* **2019**, *299*, 245−252. (i) Pan, Z.; Qiu, Y.; Yang, J.; Ye, F.; Xu, Y.; Zhang, X.; Liu, M.; Zhang, Y. Ultra-endurance flexible all-solid-state asymmetric supercapacitors based on three-dimensionally coated MnOx nanosheets on nanoporous current collectors. *Nano Energy* **2016**, *26*, 610−619. (j) Liu, Y.; Narayanasamy, M.; Yang, C.; Shi, M.; Xie, W.; Wu, H.; Yan, C.; Hou, H.; Guo, Z. High-performance coaxial wire-shaped supercapacitors using ionogel electrolyte toward sustainable energy system. *J. Mater. Res.* **2019**, *34*, 3030−3039. (k) Zhang, Z.; Xiao, F.; Wang, S. Hierarchically structured MnO2/graphene/carbon fiber and porous graphene hydrogel wrapped copper wire for fiber-based flexible all-solid-state asymmetric supercapacitors. *J. Mater. Chem. A* **2015**, *3*, 11215−11223.

https://doi.org/10.1021/acsomega.2c07075
ACS Omega 2023, 8, 6621−6631